Applied Surface Science 712 (2025) 164204

Contents lists available at ScienceDirect

Applied Surface Science

journal homepage: www.elsevier.com/locate/apsusc

Full Length Article

Nondestructive analysis of interface damage and stress in Al-ion implanted 4H-SiC homoepitaxial wafers via micro-Raman and multiscale simulation

Zhoudong Yang [a], Yuanhui Zuo [b,*], Xinyue Wang [a], Hong Zhou [a], Hongyu Tang [a], Changran Zheng [a], Rongjun Zhang [a,c,*], Zhuorui Tang [a,d], Kefeng Dai [d], Xuejun Fan [e], Guoqi Zhang [f], Jiajie Fan [a,b,f,*]

[a] Shanghai Engineering Technology Research Center of SiC Power Device, College of Intelligent Robotics and Advanced Manufacturing, Fudan University, Shanghai 200433, China
[b] Research Institute of Fudan University in Ningbo, Ningbo 315336, China
[c] School of Information Science and Technology, Fudan University, Shanghai 200433, China
[d] Ji Hua Laboratory, Foshan 528000, China
[e] Department of Mechanical Engineering, Lamar University, PO Box 10028, Beaumont, TX 77710, USA
[f] EEMCS Faculty, Delft University of Technology, Delft 2628, the Netherlands

ARTICLE INFO

Keywords:
4H-SiC
Ion implantation
Multiscale simulation
Interfacial damage
Residual stress
Micro-Raman spectroscopy

ABSTRACT

High-energy Al ion implantation is an indispensable technique for achieving precise doping in fabricating 4H-SiC devices. However, it inevitably introduces interfacial damage and residual stress that can compromise subsequent manufacturing processes and device reliability. Conventional destructive characterization techniques cannot provide real-time, in-situ, nondestructive monitoring under process conditions, creating a major bottleneck in quality control. Here, we establish a predictive modeling framework that integrates multiscale simulations with advanced, non-destructive micro-Raman spectroscopy to systematically investigate the evolution of high-energy Al ion implantation–induced interface defects and residual stress in 4H-SiC. Simulation results reveal a linear relationship between the implantation dose and the formation of vacancies and interstitial defects, while the stress accumulation tends to saturate at higher doses due to a dynamic equilibrium among defect interactions. Complementary micro-Raman spectroscopy corroborates the simulations, showing that the damaged interface layer deepens from approximately 300 nm at a dose of 10^{14} ions cm^{-2} to nearly 500 nm at 10^{16} ions cm^{-2}, consistent with Monte Carlo predictions. Furthermore, the molecular dynamics simulations capture a trend of the implantation stress evolution with strong concurrence with the Raman-measured residual stress. This combined computational–experimental approach elucidates the fundamental mechanisms governing defect formation and residual stress in ion-implanted 4H-SiC, establishes implantation dose as the pivotal role of 4H-SiC in defect density and residual stress, and underscores the utility of optical-based characterization in real-time, non-invasive quality control for advanced manufacturing.

1. Introduction

The escalating demands of modern electronic devices for high frequency, power, and temperature tolerance necessitate the development of novel semiconductor materials. Among various materials, 4H-SiC has emerged as a critical enabler for next-generation power and high-temperature applications, owing to its superior thermal conductivity, high breakdown field strength, low power loss, and remarkable thermal stability [1,2]. In device fabrication, doping is essential for tailoring material properties and constructing P-N junctions. However, the high bond energy and chemical stability of 4H-SiC result in extremely low diffusion coefficients of dopants such as Al, B, N, and P [3,4]. Enhancing the diffusion coefficient typically requires high temperatures exceeding 2000 °C, making traditional thermal diffusion methods inadequate for achieving rapid and spatially precise doping necessary in advanced 4H-SiC devices [5,6].

High-energy ion implantation provides an attractive alternative, enabling precise control over doping profiles by adjusting implantation

* Corresponding author.
E-mail addresses: zuo_yuanhui@fudan.edu.cn (Y. Zuo), rjzhang@fudan.edu.cn (R. Zhang), jiajie_fan@fudan.edu.cn (J. Fan).

https://doi.org/10.1016/j.apsusc.2025.164204
Received 27 April 2025; Received in revised form 25 July 2025; Accepted 29 July 2025
Available online 31 July 2025

energy and dose [7,8]. Despite its advantages, it introduces interfacial damage and residual stress within the lattice—factors that can adversely affect subsequent processing steps and ultimately compromise device reliability. Recent advances in simulation methodologies, such as molecular dynamics (MD) and Monte Carlo (MC) techniques, have provided valuable insights into the microscale mechanisms governing defect generation and evolution during ion implantation [9,10]. For instance, MD simulations have revealed that amorphous regions expand with increasing ion implantation dose for species such as Xe [11], H [12,13], and Cu [13] ion implantation in 4H-SiC, although the formation rate decreases. Similarly, MC simulations of proton implantation in epitaxial 4H-SiC demonstrate that variations in beam alignment conditions can precisely control the shape of the implanted dopant profile and its implantation damage [14]. These simulations provide valuable insights into the initial damage formation and its dynamic evolution, establishing a theoretical foundation for understanding the interactions between implanted ions and the lattice structure. However, experimental validation of these predictive models remains essential for a comprehensive understanding of the ion-lattice interactions. Experimental techniques to characterize implantation-induced damage and recovery include various imaging methods, such as medium-angle and high-angle annular dark-field scanning transmission electron microscopy (STEM) [15,16]. Nevertheless, the stringent specimen preparation for high-resolution electron microscopy can inevitably introduce additional defects [17,18]. To address these limitations, non-destructive characterization techniques have gained prominence. Methods include Rutherford backscattering spectroscopy [19], low-energy muon spin spectroscopy [20], deep-level transient spectroscopy [20,21], confocal micro-Raman spectroscopy [10,22,23], and synchrotron high-energy X-ray diffraction [24,25]. While these approaches have substantially improved our understanding of doping-induced lattice damage, less attention has been directed toward the role of residual stress, particularly at critical interfaces that emerge from defect accumulation [26]. Residual stress can adversely affect subsequent fabrication steps [27,28] and reduce device yield [29,30]. Therefore, clarifying the interplay between defects and residual stress is vital for optimizing ion implantation processes and improving device reliability.

Although the technology for N-type 4H-SiC is relatively mature [31], challenges persist in achieving high-quality P-type 4H-SiC [32]. Compared to B, Al has emerged as the preferred dopant for P-type doping in 4H-SiC devices owing to its low ionization energy [20]. In this work, we systematically investigate the dose-dependent evolution of interfacial damage and residual stress in Al ion implanted 4H-SiC (without post-implantation rapid thermal annealing) by integrating multiscale MD and MC simulations with high-resolution micro-Raman spectroscopy. This integrated strategy enables rapid, non-destructive, real-time prediction and monitoring of implantation-induced defects and stress fields. Crucially, it not only elucidates the nano/micro-scale mechanisms underlying defect formation and stress evolution but also validates the predictive models with experimental observations. These insights offer crucial theoretical guidance for refining ion-implantation protocols and subsequent annealing processes, underscoring the potential of photon-based, non-invasive diagnostics in advanced semiconductor manufacturing.

2. Experimental details

2.1. Sample preparation

The samples investigated in this experiment were 6-inch commercial 4H-SiC homoepitaxial wafers fabricated via chemical vapor deposition, featuring an epitaxial layer thickness of 10 μm (China Electronics Compound Semiconductor Co., Ltd., China). The Al ion implantation was conducted at 350 °C with an implantation energy of 300 keV. The implantation doses applied were 10^{11} ions cm^{-2}, 10^{14} ions cm^{-2}, and 10^{16} ions cm^{-2}, respectively. These three fluences encompass the regimes of initial damage, device process-relevant damage, and extreme damage, allowing for a systematic study of defect formation and residual-stress evolution with increasing implantation dose. Specifically, a fluence of 10^{14} ions cm^{-2} corresponds to the Al concentration routinely used in p-type 4H-SiC power devices [4,33], while 10^{16} ions cm^{-2} exceeds conventional device-level doping levels, inducing high-density defect clustering.

2.2. Characterization and measurements

Surface roughness was assessed by atomic force microscopy (AFM, Bruker/Dimension Icon, Germany). Raman spectroscopy measurements were performed using a HORIBA confocal micro-Raman spectrometer (Japan), which was calibrated with the single-crystal silicon peak at 520.7 cm^{-1}. The experiments employed a backscattering mode with a 100 × objective (N.A.: 0.90) for light collection, yielding a spot size of approximately 0.7 μm. Spectral dispersion was achieved with a 1800 gr/mm grating. The laser excitation wavelength was 532 nm, and the laser power was set to 2.5 mW to minimize the influence of thermal effects on phonon modes. To accurately extract the E_2 peak's width and position, we referred to the literature and performed spectral fitting in Python using a Gaussian–Lorentzian function [22]. Longitudinal Raman profiles were acquired at 100 nm intervals over the first 1 μm of depth and at 2 μm intervals from 1 μm to 14 μm. At each depth, spectra were recorded with a 10-second integration time and three accumulations.

2.3. Molecular dynamics simulation

Ion implantation simulations were performed on a 4H-SiC slab oriented parallel to the (0001) surface. The dimensions of the 4H-SiC slab were 10.15 nm × 10.18 nm × 17.88 nm, containing 180,576 atoms, with periodic boundary conditions applied in X and Y directions. This slab was divided into three regions: the boundary layer, the thermostatic layer, and the Newtonian layer, as shown in **Fig. S1**. The boundary layer, comprising the bottom four atomic layers, was fixed to maintain stability. The thermostatic and Newtonian layers were subjected to different ensembles: the NVT (canonical) ensemble, regulated by a Nose-Hoover thermostat, and the NVE (microcanonical) ensemble, respectively. The thermostatic layer served to dissipate the heat generated during the Al ion implantation process, with the velocities of the atoms in this region adjusted to maintain a constant temperature. Temperature regulation during ion bombardment was exclusively applied to the thermostatic layer, while the Newtonian layer was utilized to analyze the cascade collision events induced by the implanted ions, enabling the study of lattice damage distribution. Al ion implantation was simulated on the 4H-SiC surface. The ion implantation is in the yellow square region of the size of 7.5 nm × 7.5 nm. Compared to 10^{11} ions cm^{-2} and 10^{16} ions cm^{-2} implantation densities, a dose of 10^{14} ions cm^{-2} provides the best balance between statistical reliability and computational efficiency, which is consistent with previous simulation studies [11,32,34,35]. Therefore, we focused on implantation in the dose range of 0.9 × 10^{14} ions cm^{-2} to 5.4 × 10^{14} ions cm^{-2} at 2 keV. The time interval for each ion implantation was set to 20 ps. A variable timestep ranging from 0.02 fs to 1 fs was used to accurately capture the rapid movement of particles during the simulation. Atomic interactions within the 4H-SiC lattice were modeled using the GW-ZBL potential [36], while the interactions of implanted Al atoms were modeled using the embedded atom method (EAM) potential [37]. Cross-interactions between Al-Si and Al-C atoms were represented by a Morse potential developed through ab initio calculations [38]. Molecular dynamics simulations were conducted using the Large-scale Atomic/Molecular Massively Parallel Simulator (LAMMPS) package [39], and visualization and data analysis were performed using the Open Visualization Tool (OVITO) [40]. The lattice structure and defect evaluation of 4H-SiC during the simulation were conducted using the Identify Diamond Structure (IDS) method.

2.4. Monte Carlo simulation

The simulations of Al ion implantation into 4H-SiC were conducted using SRIM-2013 software with detailed calculations including full damage cascades. The threshold displacement energies for carbon and silicon were set to 20 eV and 35 eV, respectively, with a lattice binding energy of zero [11,14,41,42]. The 4H-SiC density was 3.21 g cm^{-3}. The Al ion implantation energy was 300 keV.

2.5. Definition and Calculation of roughness

This study involves three types of roughness: S_a, S_q, and R_a, and their specific definitions are as follows [43]:

(1) S_a is the arithmetic mean roughness of the surface, and the equation is:

$$S_a = \frac{1}{A}\iint_A |z(x,y)|dxdy \tag{1}$$

where A is the measured area and $z(x,y)$ is the surface height relative to the mean plane.

(2) S_q is the root mean square roughness of the surface, and the equation is:

$$S_q = \sqrt{\frac{1}{A}\iint_A [z(x,y)]^2 dA} \tag{2}$$

(3) R_a is the linear arithmetic mean roughness, and the equation is:

$$R_a = \frac{1}{L}\int_0^L |z(x)|dx \tag{3}$$

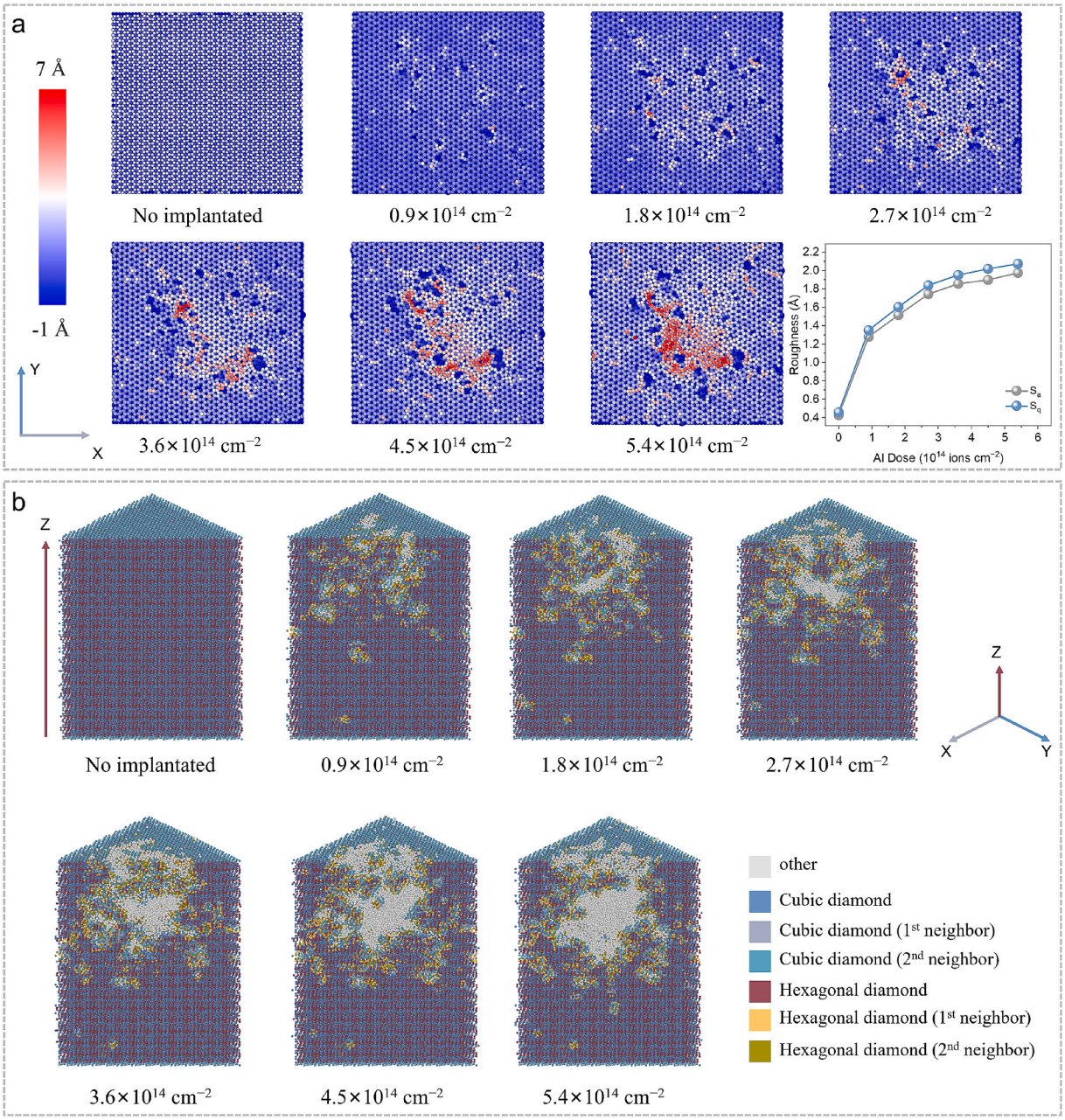

Fig. 1. Structural damage analysis of 4H-SiC under different Al ion implantation doses based on molecular dynamics simulation. **a,** Surface damage of 4H-SiC. **b,** Distribution of internal structural damage within 4H-SiC (cross section along the diagonal).

where L is the profile length and $z(x)$ is the height profile along the scan line.

3. Results and Discussion

3.1. Atomic/nano-scale simulation of Al ion implantation effects

MD simulations were conducted to examine the surface structural modifications in 4H-SiC under varying doses of Al ion implantation (Fig. 1**a**). The results reveal that Al ion beam implantation induces a sputtering effect, forming distinct pits on the surface. During implantation, Si and C atoms migrate and subsequently accumulate, leading to significant surface roughness. With increasing Al ion doses, the surface roughness becomes more pronounced, as evidenced by the rising S_a and S_q values presented in **Tab. S1**. This trend underscores the dose-dependent enhancement of surface roughness due to Al ion implantation.

The internal damage of 4H-SiC at different Al ion implantation doses was identified using the IDS method via OVITO [40], as shown in Fig. 1**b**. Initially, the 4H-SiC lattice maintains its crystalline integrity. However, with the implantation of high-energy Al ions, damage can be observed and expands with increasing Al doses. This damage is primarily localized near the surface with large amorphous clusters surrounded by smaller clusters. The correlation between surface and internal damage suggests that the displacement and migration of Si and C atoms on the surface trigger extensive cascade collisions, propagating damage deeper into the lattice. For clarity in our subsequent analysis, we define implantation depth as the average penetration distance at which ions dissipate their kinetic energy, and damage depth as the total extent of lattice disruption caused by these collision cascades [44,45].

The radial distribution function (RDF) was employed to further analyze the structural damage in 4H-SiC at different ion implantation doses. Two regions were selected for analysis: the near-surface damage concentration zone and the entire model. In the near-surface zone, the primary RDF peak, located at 1.875 Å, corresponds to the C-Si distance, closely matching the actual bond length of 1.89 Å [46], as shown in Fig. 2**a**. With increasing ion doses, the intensity of the RDF peaks decreases, indicating escalating structural damage and enhanced long-range disorder in the near-surface region. Additionally, the absence of a graphite-like peak at 1.575 Å confirms that no graphitization occurs in the 4H-SiC [47]. In contrast, the RDF analysis of the entire model reveals that higher implantation doses lead to limited lattice damage, with the long-range order of the crystal structure largely preserved, as shown in **Fig. S2**. This indicates that the overall damage to the crystal remains minimal during Al ion implantation. Statistical analysis of the Al ion depth distribution (Fig. 2**b**) reveals minimal variation across different doses, with the highest ion concentration typically occurring between 40 and 60 Å, suggesting that implantation doses have a negligible impact on the ion penetration depth. Notably, higher doses introduce asymmetries in the depth profiles, reflecting increased damage inside the crystal caused by implantation [48,49]. However, it should be noted that the finite ion energy and slab dimensions in our MD simulations can cause the predicted implantation and damage depths to differ from experimental measurements.

To quantify the extent of damage and microscopic lattice changes in 4H-SiC, Wigner-Seitz (WS) defect analysis was performed, focusing on point defects such as vacancies and interstitials [50]. This method enabled the quantification of the displacement of Si and C atoms from

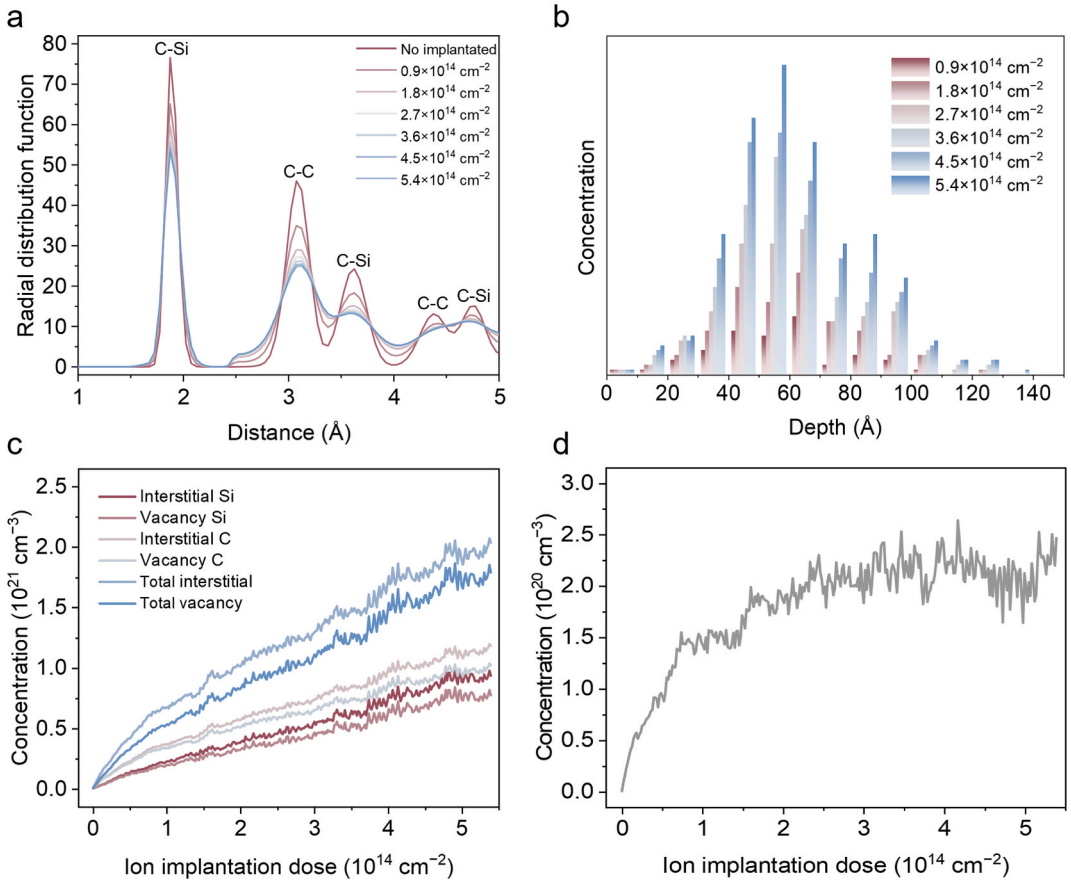

Fig. 2. Molecular dynamics simulation results at different Al ion implantation doses. **a,** Variations in the radial distribution function. **b,** Depth distribution of implanted Al ions. **c,** Trends in vacancies and interstitial atoms with increasing implantation dose. **d,** Comparison of interstitial atoms and vacancies with implantation dose.

their original lattice positions, revealing trends in the evolution of vacancy and interstitial defects. As shown in Fig. 2**c**, both vacancy and interstitial concentrations increase linearly with the Al ion dose. This linear relationship aligns with previous studies on ion implantation, confirming the correlation between implantation dose and the defect distribution in the IDS damage distribution diagram. Notably, carbon vacancies (C vacancies) are more prevalent than silicon vacancies (Si vacancies) due to the lower threshold displacement energy of C (20 eV) compared to Si (35 eV) [51]. Fig. 2**d** shows the vacancy-interstitial disparity, which exhibits a saturation trend at higher doses, highlighting an equilibrium relationship between vacancies and defects at high implantation doses in 4H-SiC [11].

Further analysis reveals the evolution of hydrostatic stress within the 4H-SiC lattice under different implantation doses (Figs. 3 **and S3**). The lattice experiences both compressive and tensile stresses, represented by negative and positive values, respectively. As the Al ion dose increases, the stress profile rapidly expands from the surface but eventually saturates at higher doses. This saturation is attributed to the balancing effects of lattice expansion caused by interstitial defects and contraction due to vacancies, which mitigate local stress concentrations and stabilize overall stress levels [52]. The average stress was calculated to provide insight into the internal stress dynamics, with compressive stress intensifying as the dose increases but gradually slowing and stabilizing (**Fig. S4**).

3.2. *Nano/micro-scale simulation of Al ion implantation effects*

We employed the MC simulation to investigate the extent of lattice damage and ion implantation profile after Al ion implantation in 4H-SiC on a larger scale. Specifically, **Fig. S5a** illustrates the trajectory of 300 keV Al ions from their entry point to their final position within the 4H-SiC lattice. Given the displacement threshold energies of Si (35 eV) and C (20 eV), the Al ions at 300 keV displace Si and C atoms from their original lattice sites, causing secondary damage through recoil collisions. These observations are consistent with our MD simulations. **Fig. S5b** further details the resulting recoil sub-cascade events, demonstrating that the implanted Al ions induce substantial atomic displacements.

The spatial distribution of atomic vacancies and substitutional collision probabilities is shown in Fig. 4**a,b**. During the implantation process, Al ions primarily generate vacancies in Si and C lattice sites while occupying interstitial positions within the lattice. **Fig. S6** shows the final distribution of Al ions within the 4H-SiC structure, indicating a prominent concentration peak at approximately 360 nm depth and a maximum penetration depth of about 500 nm, as shown in Fig. 4**c**. This finding agrees closely with Secondary Ion Mass Spectroscopy (SIMS) measurements by Linnarsson et al. for 300 keV Al implantation in 4H-SiC, which report a peak concentration near 400 nm [53].

Additionally, we analyzed the relationship between total vacancy concentration and depth under varying Al ion implantation doses. The results demonstrate a direct correlation between total vacancy concentration and implantation dose. Specifically, as the dose increased from 0.9×10^{14} ions cm^{-2} to 5.4×10^{14} ions cm^{-2}, the total vacancy concentration rose from 10^{21} cm^{-3} to 10^{22} cm^{-3} (Fig. 4**d**). To quantify lattice damage caused by Al ion implantation, we converted the total vacancies into atomic displacement per atom (dpa) values for comparative evaluation [54]:

$$\mathrm{dpa} = \left(\frac{\mathrm{vacancies}}{\mathrm{ions} \times \mathring{\mathrm{A}}}\right) \times \left(\frac{10^{8}\left(\frac{\mathring{\mathrm{A}}}{\mathrm{cm}}\right) \times \mathrm{Fluence}\left(\frac{\mathrm{ions}}{\mathrm{cm}^{2}}\right)}{N_a}\right) \tag{4}$$

where fluence (ions cm^{-2}) represents the ion flux and N_a is the atomic density ($N_a = 9.64 \times 10^{22}$ atoms cm^{-3}).

The results show that, across different ion implantation doses, the maximum dpa value caused by Al ions gradually increases from 0.5 to

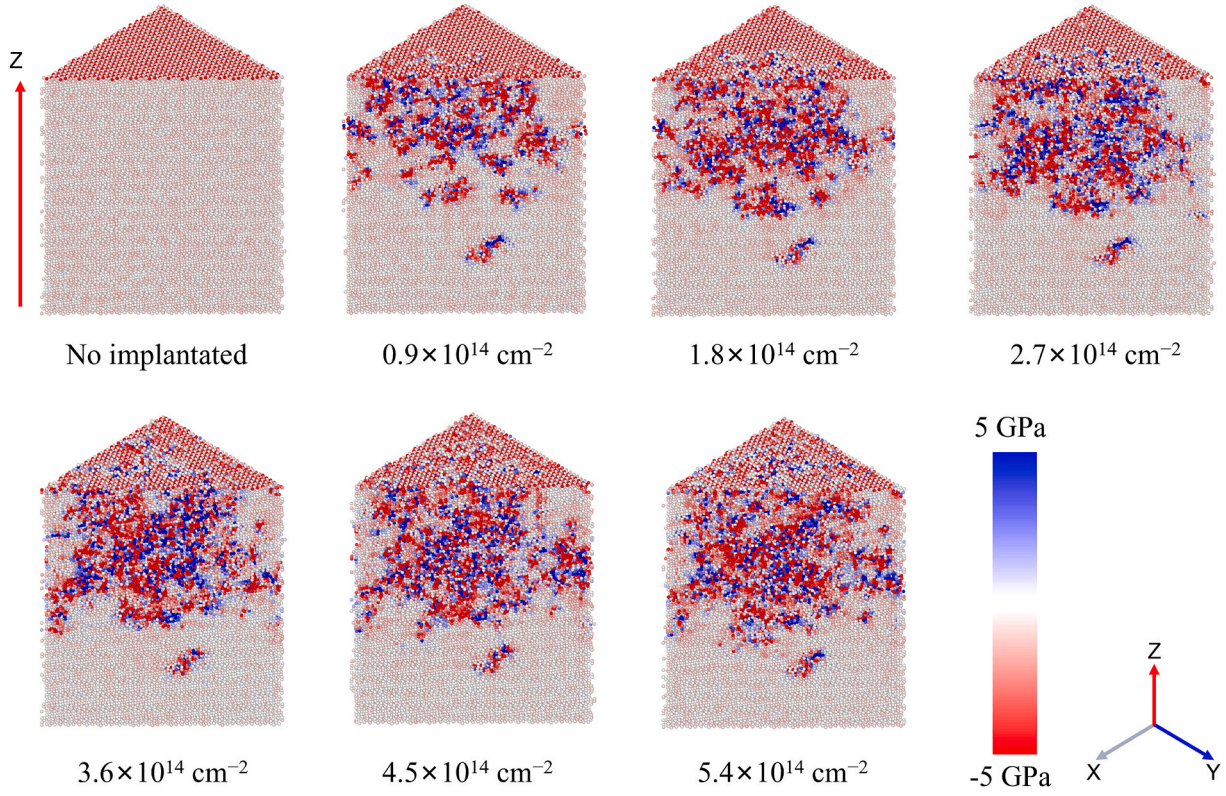

Fig. 3. Diagonal cross-sectional map of average hydrostatic stress distribution within the 4H-SiC crystal under different Al ion implantation doses based on molecular dynamics simulation.

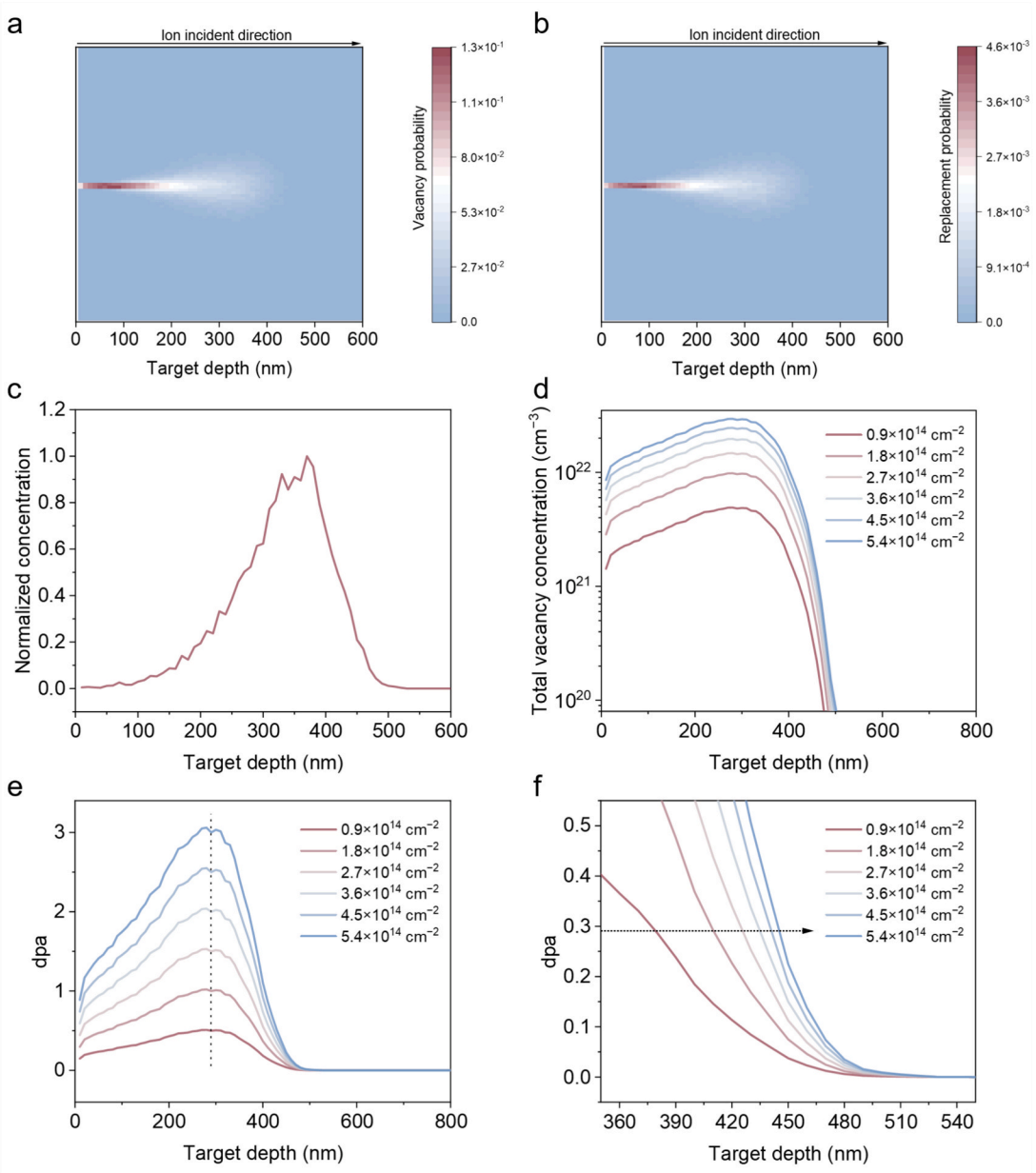

Fig. 4. Monte Carlo simulation results at different Al ion implantation doses. **a,** Probability of atomic vacancy collisions caused by Al ion implantation. **b,** Probability of atomic substitutional collisions caused by Al ion implantation. **c,** Depth concentration distribution of Al ions. **d,** Variation in vacancy concentration with implantation dose. **e,** Damage in terms of displacement per atom under different implantation doses. **f,** Changes in amorphization damage depth with implantation dose.

3.0 dpa, while the peak depth remains constant at around 280 nm (Fig. 4**e**). This further indicates that implantation depth is relatively insensitive to dose variations. Since the threshold for 4H-SiC amorphization is approximately 0.28 dpa [42], these implantation doses result in amorphization damage. Fig. 4**f** demonstrates that as the implantation dose increases, the extent of amorphization damage also increases, extending from a depth of approximately 380 nm at 0.9 × 10^{14} ions cm^{-2} to approximately 450 nm at 5.4 × 10^{14} ions cm^{-2}. The MC simulation results at the micro/nanoscale are consistent with those from the MD simulations, confirming that the ion implantation dose primarily affects lattice damage, with minimal impact on the implantation depth.

3.3. Experimental characterization and validation

To validate the accuracy of our simulation results regarding Al ion implantation in 4H-SiC, we conducted experiments on 6-inch 4H-SiC epitaxial wafers. Al ions were implanted at doses of 10^{11} ions cm^{-2}, 10^{14} ions cm^{-2}, and 10^{16} ions cm^{-2}, with the non-implanted wafer serving as the blank sample. Non-destructive characterization techniques were utilized to analyze the resultant damage and stress evolution under these conditions.

3.3.1. Lattice damage

The surface roughness of both the control and implanted samples was measured using AFM over a scanning area of 2 μm × 2 μm. As shown in Fig. 5**a**, the blank sample exhibited a high-quality and smooth surface. To assess the impact of ion implantation on surface flatness, line roughness was evaluated along the direction of maximum height variation within the test area (**Fig. S7**). For the sample implanted with a dose of 10^{11} ions cm^{-2}, the R_a was measured at 0.235 nm, indicating that low-dose Al ion implantation minimally affects the 4H-SiC lattice structure. As the implantation dose increased, a significant rise in surface roughness was observed. Specifically, for a dose of 10^{14} ions cm^{-2}, R_a increased to 0.300 nm, and further to 0.319 nm at the highest

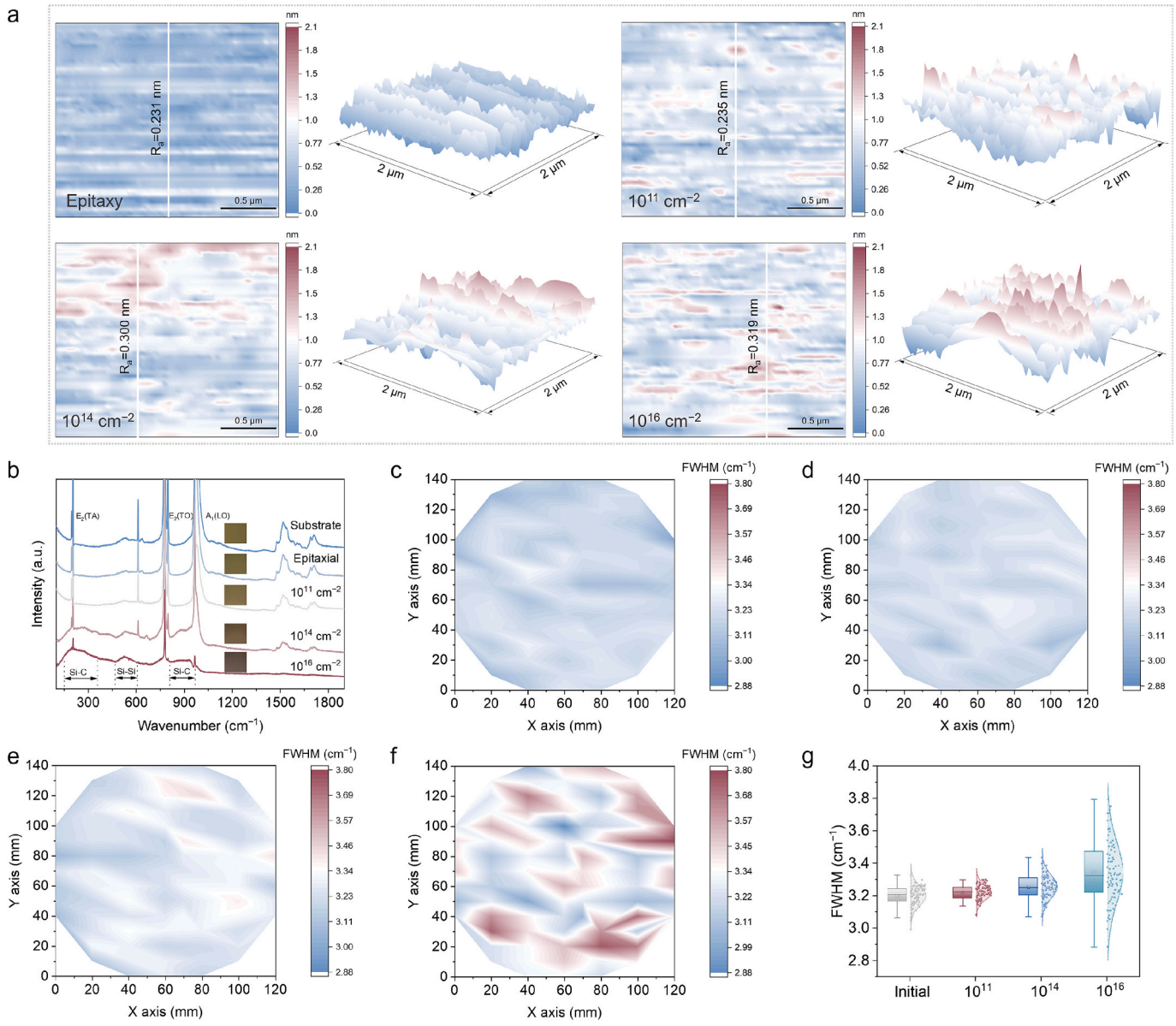

Fig. 5. Atomic force microscopy and Raman spectroscopy analysis at different Al ion implantation doses. **a,** Surface morphology of samples under varying ion implantation doses. **b,** Raman spectra of 4H-SiC at different implantation doses. Full width at half maximum (FWHM) mapping of the E_2(TO) Raman characteristic peak for **c,** No ion implantation, **d,** 10^{11} ions cm^{-2}, **e,** 10^{14} ions cm^{-2}, and **f,** 10^{16} ions cm^{-2}. **g,** Statistical analysis of FWHM distribution for the E_2(TO) peak across all samples.

implantation dose of 10^{16} ions cm^{-2}. These experimental data exhibit a strong correspondence with the surface damage trends forecast by our simulations.

Raman spectroscopy was employed to further elucidate these changes in R_a under different implantation doses (Figs. 5**b and S8**). The pristine 4H-SiC crystal exhibited characteristic Raman peaks, including the longitudinal acoustic modes E_2(LA) and A_1(LA) characteristic peaks at 195 cm^{-1} and 610 cm^{-1}, respectively; the transverse acoustic mode E_2(TA) at 210 cm^{-1}; the transverse optical modes E_2(TO) and E_1(TO) at 777 cm^{-1} and 797 cm^{-1}; and the characteristic peak at 967 cm^{-1} corresponds to the longitudinal optical mode A_1(LO) [55–57]. With increasing ion implantation doses, the intensity of these peaks gradually diminished, with the A_1(LA) mode eventually disappearing. This reduction in intensity is attributed to decreased Raman polarizability due to bond breaking and changes in atomic forces and displacements [58]. Additionally, broad peaks emerged in the regions of 150–350 cm^{-1}, 470–600 cm^{-1}, and 810–960 cm^{-1}, with their intensities increasing with higher doses. These broad peaks generally arise from changes in the internal structural order of the material [59]. Specifically, the broad peak at 470–600 cm^{-1} is attributed to the Si-Si bond in amorphous silicon, while the broad peaks at 150–350 cm^{-1} and 810–960 cm^{-1} correspond to the Si-C bond in amorphous silicon carbide [60,61].

The optical images of different samples corroborate the Raman results, showing a color change from transparent light green to opaque dark brown with increasing ion implantation dose (**Fig. S9**). This color change is attributed to the formation of an amorphous surface layer and modification of the electron energy levels due to ion implantation. Given that the E_2(TO) mode dominates the 4H-SiC Raman spectrum, we used its full width at half maximum (FWHM) and peak intensity as indicators of lattice quality. Multi-point Raman scanning across different samples revealed that the FWHM value tended to increase with increasing implantation dose (Fig. 5**c-f**). Statistical analysis in Fig. 5**g** shows that the blank sample had a low and relatively concentrated FWHM value of

approximately 3.2 cm^{-1}. In the low-dose sample, the FWHM value increased slightly while remaining relatively uniform. However, for the high-dose sample (10^{16} ions cm^{-2}), the FWHM distribution became more dispersed, reflecting a significant increase in surface amorphization. The evolution of Raman peak intensity was opposite to the FWHM trend, showing a gradual decrease with increasing dose (Fig. S10).

MC simulations suggest that ion implantation damage primarily occurs within the top 1 μm of the surface. To further investigate near-surface lattice damage, we performed longitudinal tests from the surface to a depth of 1 μm at 100 nm intervals based on high spatial resolution confocal micro-Raman (Fig. 6**a**) [62]. For the low-dose sample (10^{11} ions cm^{-2}), no significant amorphous features were detected, indicating that the implantation-induced lattice damage did not reach the amorphization threshold of 4H-SiC, and the crystal structure remained largely intact. At a dose of 10^{14} ions cm^{-2}, characteristic amorphous peaks emerged near the surface (amorphized Si-Si bond: 470–600 cm^{-1}; amorphized Si-C bond: 150–350 cm^{-1} and 810–960 cm^{-1}). These peaks weakened with increasing depth and disappeared at approximately 300 nm, indicating the thickness of the amorphous damage layer. When the dose increased to 10^{16} ions cm^{-2}, the intensity of the amorphous peaks significantly increased, and the amorphous layer thickness extended to approximately 500 nm. MC simulations further quantified the thickness of the amorphous damaged layer under different implantation doses (Fig. S11). For the sample dosed at 10^{11} ions cm^{-2}, the dpa value was far below the amorphization threshold of 0.28, resulting in no detectable amorphous damage layer. In contrast, the dpa values of the samples implanted with 10^{14} ions cm^{-2} and 10^{16} ions cm^{-2} exceeded this threshold, leading to amorphous damage layers

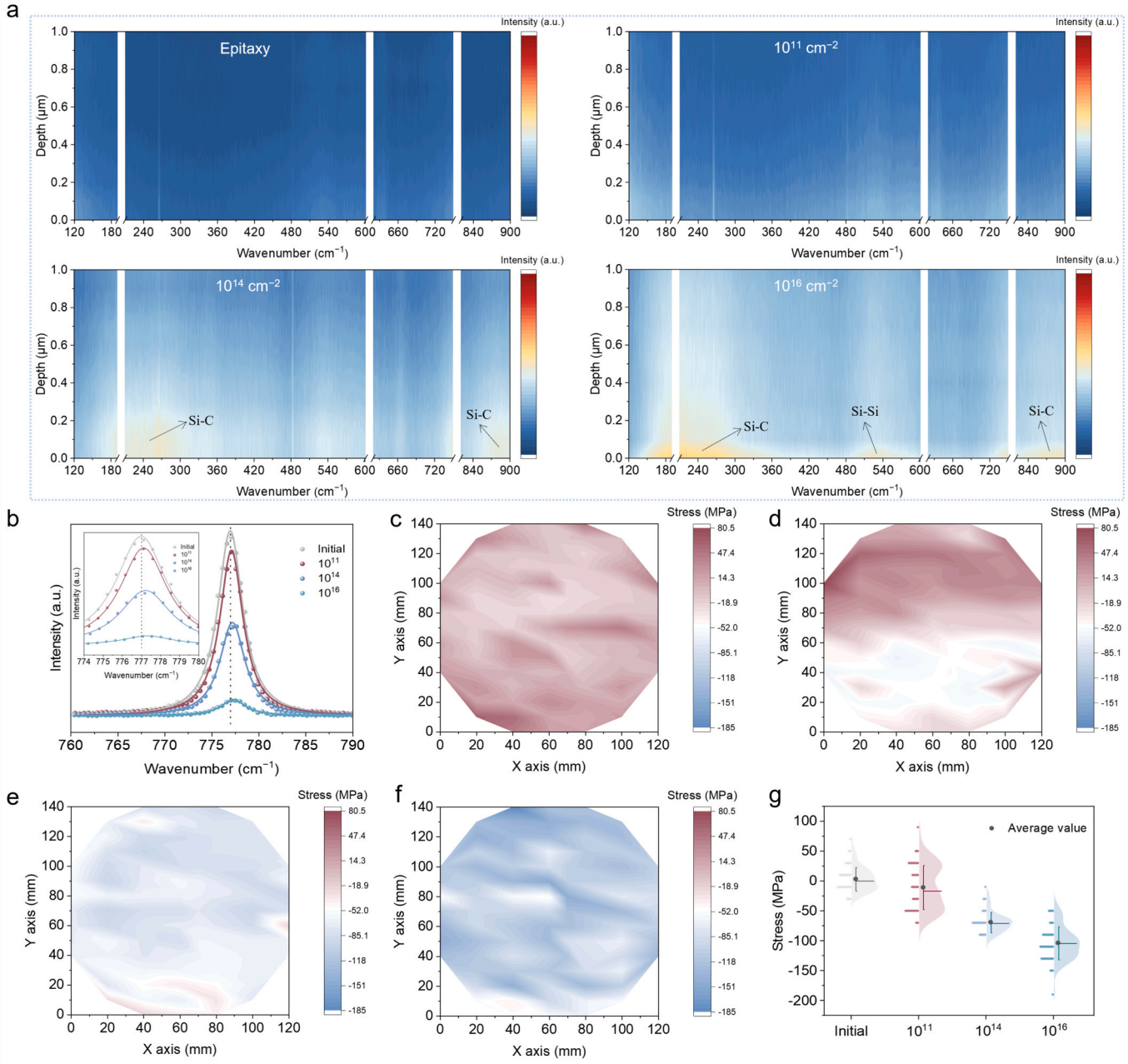

Fig. 6. Longitudinal confocal micro-Raman linear scans and residual stress analysis under different Al ion implantation doses. **a,** Longitudinal Raman spectra of each sample within a 1 μm depth. **b,** Shift in the E_2(TO) Raman characteristic peak of 4H-SiC with varying implantation doses. Stress mapping for each sample: **c,** No ion implantation, **d,** 10^{11} ion cm^{-2}, **e,** 10^{14} ion cm^{-2}, and **f,** 10^{16} ion cm^{-2}. **g,** Statistical analysis of stress distribution for each sample.

of approximately 380 nm and 490 nm, respectively. These simulation results closely matched those obtained from confocal depth profiling. To confirm that ion implantation-induced lattice damage was confined within the top 1 μm, we extended the confocal depth scans beyond 1 μm in 2 μm intervals up to 14 μm. The Raman spectra of each sample beyond 1 μm are consistent with the standard 4H-SiC spectrum, indicating no significant changes with increasing depth (**Fig. S12**).

3.3.2. Residual stress

Raman spectroscopy is a reliable and efficient method for analyzing material stress [63,64]. We further employed confocal micro-Raman spectroscopy to assess in-plane stress by focusing on the peak shift of the E_2(TO) mode ($\Delta\omega$), which is typically sensitive to plane stress. First, to exclude the fitting deviation caused by the asymmetry of the Raman peak, we compared the difference between the Gaussian-Lorentz fitting and the Fano fitting (considering the peak asymmetry) [65,66], as shown in **Tab. S2**. The difference between the Gaussian-Lorentz fitting and the Fano fitting results is less than 0.02 cm^{-1} in peak position, and the FWHM is less than 0.15 cm^{-1}, which is much smaller than the residual stress/damage difference amplitude we are concerned about in the analysis. Therefore, within the ion implantation dose range of this study, it is reasonable to use the Gaussian-Lorentz fitting [22]. As shown in Fig. 6**b**, the blank sample's E_2(TO) peak is positioned at 777 cm^{-1}. After ion implantation, a noticeable blue shift in the E_2(TO) peak is observed (peak shift ranges from ~ 0.1 to ~ 0.3 cm^{-1}), indicating the development of compressive stress within the material. This compressive stress arises mainly due to the high-energy ion implantation into the lattice gap, resulting in local lattice distortion [67]. Moreover, disparities in atomic radii and chemical properties contribute to residual strain and significant compressive stress [68].

The specific numerical relationship between Raman shift and lattice deformation is established through the lattice dynamics theory. This theory describes the change of atomic spacing under stress and its characteristic equation [63]:

$$\begin{vmatrix} \varepsilon_{uv}K_{uv11}-\lambda & \varepsilon_{uv}K_{uv12} & \varepsilon_{uv}K_{uv31} \\ \varepsilon_{uv}K_{uv12} & \varepsilon_{uv}K_{uv22}-\lambda & \varepsilon_{uv}K_{uv32} \\ \varepsilon_{uv}K_{uv31} & \varepsilon_{uv}K_{uv32} & \varepsilon_{uv}K_{uv33}-\lambda \end{vmatrix} = 0 \tag{5}$$

where K_{uvwx} are the components of the phonon deformation tensor, dependent on the crystal structure and the optical phonon modes ($u, v = 1, 2, 3$). The anisotropic deformation of the crystal is characterized by strain tensors (ε_{11}, ε_{22}, and ε_{33}) along specific axes (X, Y, and Z). Additionally, ε_{12}, ε_{23}, and ε_{13} represent the strain tensors along the XY, YZ, and XZ planes, respectively.

To establish the specific numerical equation of Raman shift and stress, we first define the [1–100], [11–20], and [0001] crystal directions of 4H-SiC crystal as X, Y, and Z axes, respectively. For 4H-SiC, which has a hexagonal crystal structure, the Raman tensor of its E_2(TO) mode shows double degeneracy [69]:

$$R^1_{E_2} = \begin{pmatrix} 0 & d & 0 \\ d & 0 & 0 \\ 0 & 0 & 0 \end{pmatrix}, R^2_{E_2} = \begin{pmatrix} d & 0 & 0 \\ 0 & -d & 0 \\ 0 & 0 & 0 \end{pmatrix} \tag{6}$$

Therefore, the characteristic equation of lattice dynamics simplifies to [70]:

$$\begin{vmatrix} a_{E_2}(\varepsilon_{11}+\varepsilon_{22})+b_{E_2}\varepsilon_{33}+c_{E_2}(\varepsilon_{11}-\varepsilon_{22})-\Delta\omega_{E_2} & 2c_{E_2}\varepsilon_{12} \\ 2c_{E_2}\varepsilon_{12} & a_{E_2}(\varepsilon_{11}+\varepsilon_{22})+b_{E_2}\varepsilon_{33}-c_{E_2}(\varepsilon_{11}-\varepsilon_{22})-\Delta\omega_{E_2} \end{vmatrix} = 0 \tag{7}$$

where a_{E2}, b_{E2}, and c_{E2} are the phonon deformation potential constants of the E_2(TO) mode.

The relationship between Raman shift and strain for 4H-SiC is derived as:

$$\Delta\omega_{E_2} = a_{E_2}(\varepsilon_{11}+\varepsilon_{22}) + b_{E_2}\varepsilon_{33} \pm c_{E_2}\sqrt{(\varepsilon_{11}-\varepsilon_{22})^2+4\varepsilon_{12}^2} \tag{8}$$

The measured 4H-SiC is in an in-plane stress state: [70]

$$\Delta\sigma = \begin{pmatrix} \Delta\sigma_{11} \\ \Delta\sigma_{22} \\ 0 \\ 0 \\ 0 \\ \Delta\sigma_{12} \end{pmatrix} \tag{9}$$

Combining generalized Hooke's law, the stress–strain equation of 4H-SiC under the in-plane stress state is obtained:

$$\begin{pmatrix} \varepsilon_{11} \\ \varepsilon_{22} \\ \varepsilon_{33} \\ 2\varepsilon_{23} \\ 2\varepsilon_{31} \\ 2\varepsilon_{12} \end{pmatrix} = \begin{pmatrix} s_{11} & s_{12} & s_{13} & & & \\ s_{12} & s_{11} & s_{13} & & & \\ s_{13} & s_{13} & s_{33} & & & \\ & & & s_{44} & & \\ & & & & s_{44} & \\ & & & & & s_{66} \end{pmatrix} \begin{pmatrix} \Delta\sigma_{11} \\ \Delta\sigma_{22} \\ 0 \\ 0 \\ 0 \\ \Delta\sigma_{12} \end{pmatrix} = \begin{pmatrix} s_{11}\Delta\sigma_{11}+s_{12}\Delta\sigma_{22} \\ s_{12}\Delta\sigma_{11}+s_{11}\Delta\sigma_{22} \\ s_{13}(\Delta\sigma_{11}+\Delta\sigma_{22}) \\ 0 \\ 0 \\ s_{66}\Delta\sigma_{12} \end{pmatrix} \tag{10}$$

Combining **Eqs. (8) and (10)**, the relationship between the Raman shift and stress is obtained:

$$\Delta\omega_{E_2} = a'_{E_2}(\Delta\sigma_{11}+\Delta\sigma_{22}) \pm c'_{E_2}\sqrt{(\Delta\sigma_{11}-\Delta\sigma_{22})^2+4\Delta\sigma_{12}^2} \tag{11}$$

And the a'_{E2}, and c'_{E2} correspond to the phonon deformation potential constants a_{E2}, b_{E2} and c_{E2} through the following equations:

$$\begin{aligned} a'_{E_2} &= a_{E_2}(s_{11}+s_{12})+b_{E_2}s_{13} \\ c'_{E_2} &= c_{E_2}\sqrt{\frac{s_{66}^2}{4}} = c_{E_2}|s_{11}-s_{12}| \end{aligned} \tag{12}$$

where a'_{E2} and c'_{E2} are − 1.55 cm^{-1} GPa^{-1} and 0.37 cm^{-1} GPa^{-1}, respectively [71].

For a spherical thin block, the in-plane stress is modeled as equi-biaxial stress ($\Delta\sigma_{11} = \Delta\sigma_{22} \neq 0$, $\Delta\sigma_{12} = 0$), leading to the following relationship:

$$\Delta\omega_{\text{obs}} = \Delta\omega_1 = \Delta\omega_2 = 2a'_{E_2}\Delta\sigma_{\text{in-plane}} \tag{13}$$

Finally, the numerical equation of Raman shift and stress in the biaxial stress model for 4H-SiC is obtained:

$$\Delta\sigma_{\text{in-plane}}(\text{MPa}) = -323\Delta\omega_{\text{obs}}(\text{cm}^{-1}) \tag{14}$$

To determine the stress-free Raman shift (ω_0), eight points on a 4H-SiC single crystal were measured, yielding the E_2(TO) mode peak position of 776.97 ± 0.07 cm^{-1}. This established a reference peak position of 777 cm^{-1} for the stress-free state (**Fig. S13**). Raman mapping was performed on the surface area of each sample, specifically including 15 rows (1 cm row spacing) and 7 columns (2 cm column spacing) with a total of 85 test points, as shown in **Fig. S14**. The distribution of peak

shifts for each sample is shown in Fig. S15. Stress distribution across the tested regions was then analyzed using **Eq. (14)** (Fig. 6**c**-g). The epitaxial wafer exhibited negligible internal stress, in contrast to ion-implanted samples, which predominantly exhibited compressive stress. At a lower implantation dose of 10^{11} ions cm^{-2}, the stress increase was negligible compared to the blank sample. However, as the dose increased to 10^{14} and 10^{16} ions cm^{-2}, the compressive stress significantly intensified, peaking at about −97 MPa and −185 MPa, respectively. The variation in internal stress with different ion implantation doses closely matched trends predicted by MD simulations for average stress (Fig. S16). These results underscore the crucial role of implantation dose in stress formation within 4H-SiC, which is primarily driven by defect generation leading to pronounced lattice distortion and stress development.

4. Conclusion

In summary, this work systematically investigated the impact of high-energy Al ion implantation on interfacial damage and residual stress in 4H-SiC by integrating MD and MC simulations with nondestructive micro-Raman spectroscopy. Our findings reveal that Al implantation predominantly generates interstitial defects over vacancy defects, leading to net compressive stress within the implanted region that saturates with increasing doses. MC simulations indicate that while the implantation depth of implanted Al is independent of the implantation dose, the depth of lattice damage increases with higher doses. These findings are strongly corroborated by micro-Raman measurements, which emphasize the critical role of implantation dose in dictating both defect accumulation and stress distribution. By leveraging the complementary strengths of multiscale simulations and non-destructive optical diagnostics, this work elucidates the fundamental mechanisms governing Al ion implantation dose-induced defect formation and stress evolution in 4H-SiC. Moreover, the demonstrated efficacy of micro-Raman spectroscopy highlights its potential as a high-resolution, in-situ tool for advancing quality control and performance reliability in semiconductor devices. Looking forward, coupling this approach with SIMS and other characterization techniques during post-implantation annealing will be essential for understanding damage recovery, stress relaxation, and dopant activation, thereby informing optimized implantation and annealing protocols.

CRediT authorship contribution statement

Zhoudong Yang: Writing – original draft, Visualization, Investigation, Formal analysis, Data curation. **Yuanhui Zuo:** Project administration, Funding acquisition, Data curation. **Xinyue Wang:** Writing – review & editing, Formal analysis. **Hong Zhou:** Data curation. **Hongyu Tang:** Writing – review & editing. **Changran Zheng:** Writing – review & editing. **Rongjun Zhang:** Resources. **Zhuorui Tang:** Resources. **Kefeng Dai:** Resources. **Xuejun Fan:** Supervision, Conceptualization. **Guoqi Zhang:** Software, Resources. **Jiajie Fan:** Writing – review & editing, Validation, Supervision, Software, Resources, Project administration, Methodology, Funding acquisition, Conceptualization.

Declaration of competing interest

The authors declare that they have no known competing financial interests or personal relationships that could have appeared to influence the work reported in this paper.

Acknowledgments

This work was partially supported by the National Natural Science Foundation of China (52275559 and 62401157) and the Merit-based Zhejiang Province Postdoctoral Research Project (ZJ2023118). Part of the experimental work was carried out at the Fudan Nanofabrication Laboratory. Chat Generative Pre-Trained Transformer (ChatGPT, OpenAI) for language polishing help.

Appendix A. Supplementary data

Supplementary data to this article can be found online at https://doi.org/10.1016/j.apsusc.2025.164204.

Data availability

Data will be made available on request.

References

[1] T.A. Pham, A. Qamar, T. Dinh, M.K. Masud, M. Rais-Zadeh, D.G. Senesky, Y. Yamauchi, N.T. Nguyen, H.P. Phan, Nanoarchitectonics for wide bandgap semiconductor nanowires: Toward the next generation of nanoelectromechanical systems for environmental monitoring, Adv. Sci. 7 (21) (2020) 2001294, https://doi.org/10.1002/advs.202001294.
[2] C.-C. Tu, C.-L. Hung, K.-B. Hong, S. Elangovan, W.-C. Yu, Y.-S. Hsiao, W.-C. Lin, R. Kumar, Z.-H. Huang, Y.-H. Hong, Y.-K. Hsiao, R.-H. Horng, B.-Y. Tsui, T.-L. Wu, J.-H. He, H.-C. Kuo, Industry perspective on power electronics for electric vehicles, Nat. Rev. Electr. 1 (7) (2024) 435–452, https://doi.org/10.1038/s44287-024-00055-4.
[3] A. Hallén, M. Linnarsson, Ion implantation technology for silicon carbide, Surf. Coat. Technol. 306 (2016) 190–193, https://doi.org/10.1016/j.surfcoat.2016.05.075.
[4] F. Roccaforte, P. Fiorenza, M. Vivona, G. Greco, F. Giannazzo, Selective doping in silicon carbide power devices, Materials (basel) 14 (14) (2021), https://doi.org/10.3390/ma14143923.
[5] I. Choi, H.Y. Jeong, H. Shin, G. Kang, M. Byun, H. Kim, A.M. Chitu, J.S. Im, R. S. Ruoff, S.Y. Choi, K.J. Lee, Laser-induced phase separation of silicon carbide, Nat. Commun. 7 (2016) 13562, https://doi.org/10.1038/ncomms13562.
[6] Y. Zhai, H. Li, H. Wu, Z. Tao, G. Xu, X. Cao, T. Xu, Application of bulk silicon carbide technology in high temperature MEMS sensors, Mater. Sci. Semicond. Process. 173 (2024), https://doi.org/10.1016/j.mssp.2024.108137.
[7] Y. Kang, Y. Pei, D. He, H. Xu, M. Ma, J. Yan, C. Jiang, W. Li, X. Xiao, Spatially selective p-type doping for constructing lateral WS_2 p-n homojunction via low-energy nitrogen ion implantation, Light Sci. Appl. 13 (1) (2024) 127, https://doi.org/10.1038/s41377-024-01477-3.
[8] A. Herklotz, Z. Gai, Y. Sharma, A. Huon, S.F. Rus, L. Sun, J. Shen, P.D. Rack, T. Z. Ward, Designing magnetic anisotropy through strain doping, Adv. Sci. 5 (11) (2018) 1800356, https://doi.org/10.1002/advs.201800356.
[9] R. Nipoti, H.M. Ayedh, B.G. Svensson, Defects related to electrical doping of 4H-SiC by ion implantation, Mater. Sci. Semicond. Process. 78 (2018) 13–21, https://doi.org/10.1016/j.mssp.2017.10.021.
[10] Y. Yang, C. Zhang, C. Su, Z. Ding, Y. Song, Damage and recovery behavior of 4H-SiC implanted with He ions, Nucl. Instrum. Meth. B 449 (2019) 54–57, https://doi.org/10.1016/j.nimb.2019.04.055.
[11] Y. Fan, Z. Xu, C. Yang, Z. Yang, K. Zhang, S. Zheng, Xenon ion implantation induced defects and amorphization in 4H–SiC: Insights from MD simulation and Raman spectroscopy characterization, Ceram. Int. 49 (16) (2023) 26654–26664, https://doi.org/10.1016/j.ceramint.2023.05.200.
[12] Q. Kang, X. Fang, C. Wu, P. Verma, H. Sun, B. Tian, L. Zhao, S. Wang, N. Zhu, R. Maeda, Z. Jiang, Mechanical properties and indentation-induced phase transformation in 4H–SiC implanted by hydrogen ions, Ceram. Int. 48 (11) (2022) 15334–15347, https://doi.org/10.1016/j.ceramint.2022.02.067.
[13] X. Fang, X. Wu, Q. Kang, Z. Fang, H. Sun, C. Wu, Z. Zhang, P. Verma, R. Maeda, B. Tian, C. Kang, Atomistic analysis on implantation effects of hydrogen ions and copper ions into 4H-SiC, Appl. Surf. Sci. 665 (2024), https://doi.org/10.1016/j.apsusc.2024.160329.
[14] O. Samperi, A. Azarov, V. Bobal, M. Bertolini, M. Cantiano, L. Vines, A. Hallén, S. Coffa, M.E. Fragalà, Effects of ion channelling on 350 keV proton implantation of 4H-SiC measured by D-SIMS and DLTS defect profiling, Mater. Sci. Semicond. Process. 190 (2025), https://doi.org/10.1016/j.mssp.2025.109320.
[15] C. Calabretta, A. Pecora, M. Agati, A. Muoio, V. Scuderi, S. Privitera, R. Reitano, S. Boninelli, F. La Via, Exploring crystal recovery and dopant activation in coated laser annealing on ion implanted 4H–SiC epitaxial layers, Mater. Sci. Semicond. Process. 174 (2024), https://doi.org/10.1016/j.mssp.2024.108175.
[16] L. Kuebler, E. Hershkovitz, D. Kouzminov, H.J. Gossmann, S. Charnvanichborikarn, C. Hatem, H. Kim, K.S. Jones, 4H to 3C polytypic transformation in Al^+ implanted SiC during high temperature annealing, Electron. Mater. Lett. 20 (3) (2023) 345–351, https://doi.org/10.1007/s13391-023-00473-w.
[17] F. Hofmann, E. Tarleton, R.J. Harder, N.W. Phillips, P.W. Ma, J.N. Clark, I. K. Robinson, B. Abbey, W. Liu, C.E. Beck, 3D lattice distortions and defect structures in ion-implanted nano-crystals, Sci. Rep. 7 (2017) 45993, https://doi.org/10.1038/srep45993.
[18] R. Wirth, Focused Ion Beam (FIB) combined with SEM and TEM: Advanced analytical tools for studies of chemical composition, microstructure and crystal structure in geomaterials on a nanometre scale, Chem. Geol. 261 (3–4) (2009) 217–229, https://doi.org/10.1016/j.chemgeo.2008.05.019.

[19] G. Gupta, P. Jozwik, S. Ojha, G.R. Umapathy, A. Pandey, S. Rath, Depth profiling of the Si ion implantation induced disorder and strain in 4H-SiC and the thermal annealing recovery, Appl. Surf. Sci. 665 (2024), https://doi.org/10.1016/j.apsusc.2024.160296.

[20] P. Kumar, M.I.M. Martins, M.E. Bathen, T. Prokscha, U. Grossner, Al-implantation induced damage in 4H-SiC, Mater. Sci. Semicond. Process. 174 (2024) 108241, https://doi.org/10.1016/j.mssp.2024.108241.

[21] H. Fujii, M. Kaneko, T. Kimoto, Depth profiles of deep levels generated in the tail region of Al ion implantation into n-type 4H-SiC, Jpn. J. Appl. Phys. 63 (6) (2024), https://doi.org/10.35848/1347-4065/ad4f3a.

[22] Y. Song, Z. Xu, M. Rommel, G.V. Astakhov, G. Hlawacek, F. Fang, Defects distribution and evolution in selected-area helium ion implanted 4H–SiC, Ceram. Int. 50 (5) (2024) 7691–7701, https://doi.org/10.1016/j.ceramint.2023.12.096.

[23] S. Yang, S. Tokunaga, M. Kondo, Y. Nakagawa, T. Shibayama, Non-destructive evaluation of the strain distribution in selected-area He^+ ion irradiated 4H-SiC, Appl. Surf. Sci. 500 (2020), https://doi.org/10.1016/j.apsusc.2019.144051.

[24] Z. Chen, Y. Liu, Q. Cheng, S. Hu, B. Raghothamachar, M. Dudley, Analysis of strain in ion implanted 4H-SiC by fringes observed in synchrotron X-ray topography, J. Cryst. Growth 627 (2024), https://doi.org/10.1016/j.jcrysgro.2023.127535.

[25] N.A. Mahadik, H. Das, S. Stoupin, R.E. Stahlbush, P.L. Bonanno, X. Xu, V. Rengarajan, G.E. Ruland, Evolution of lattice distortions in 4H-SiC wafers with varying doping, Sci. Rep. 10 (1) (2020) 10845, https://doi.org/10.1038/s41598-020-67900-y.

[26] S. Takitani, A. Baba, H. Nishizawa, K. Suzuki, An efficient polishing process for silicon carbide using ion implantation method, Jpn. J. Appl. Phys. 63 (3) (2024), https://doi.org/10.35848/1347-4065/ad308c.

[27] H. Wang, Z. Dong, R. Kang, S. Gao, Surface characteristics and material removal mechanisms during nanogrinding on C-face and Si-face of 4H-SiC crystals: Experimental and molecular dynamics insights, Appl. Surf. Sci. 665 (2024), https://doi.org/10.1016/j.apsusc.2024.160293.

[28] Y. Wang, H. Ding, N. Wang, Y. Huang, Y. Yu, H. Huang, N. Duan, Effect of dislocation defects on the nano-scratching process of 4H–SiC, Wear 546–547 (2024), https://doi.org/10.1016/j.wear.2024.205343.

[29] Y. Huang, R. Wang, D. Yang, X. Pi, Impurities in 4H silicon carbide: Site preference, lattice distortion, solubility, and charge transition levels, J. Appl. Phys. 135 (19) (2024), https://doi.org/10.1063/5.0190242.

[30] Q. Zeng, Z. Yang, X. Wang, S. Li, F. Gao, Research progress on radiation damage mechanism of SiC MOSFETs under various irradiation conditions, IEEE Trans. Electron Devices 71 (3) (2024) 1718–1727, https://doi.org/10.1109/ted.2024.3359172.

[31] P.V. Raja, C. Raynaud, B. Asllani, H. Morel, D. Planson, Electrically active traps in 4H-silicon carbide (4H-SiC) PiN power diodes, J. Mater. Chem. C 34 (17) (2023) 1383, https://doi.org/10.1007/s10854-023-10813-z.

[32] J. Wu, Z. Xu, L. Liu, A. Hartmaier, M. Rommel, K. Nordlund, T. Wang, R. Janisch, J. Zhao, MD simulation study on defect evolution and doping efficiency of p-type doping of 3C-SiC by Al ion implantation with subsequent annealing, J. Mater. Chem. C 9 (7) (2021) 2258–2275, https://doi.org/10.1039/d0tc05374k.

[33] F. Roccaforte, F. Giannazzo, G. Greco, Ion Implantation Doping in Silicon Carbide and Gallium Nitride Electronic Devices, Micro 2 (1) (2022) 23–53, https://doi.org/10.3390/micro2010002.

[34] Y. Fan, Y. Song, Z. Xu, B. Dong, J. Wu, M. Rommel, K. Zhang, J. Zhao, R. Zhu, B. Li, Q. Li, F. Fang, Molecular dynamics simulation of color centers in silicon carbide by helium and dual ion implantation and subsequent annealing, Ceram. Int. 47 (17) (2021) 24534–24544, https://doi.org/10.1016/j.ceramint.2021.05.172.

[35] Q. Kang, X. Fang, C. Wu, H. Sun, B. Tian, L. Zhao, S. Wang, Z. Jiang, N. Zhu, R. Maeda, M. Zhang, Y. Lv, Modification mechanism of collaborative ions implanted into 4H-SiC by atomic simulation and experiment, Int. J. Mech. Sci. 212 (2021), https://doi.org/10.1016/j.ijmecsci.2021.106832.

[36] F. Gao, W.J. Weber, Empirical potential approach for defect properties in 3C-SiC, Nucl. Instrum. Meth. B 191 (1–4) (2002) 504–508, https://doi.org/10.1016/s0168-583x(02)00600-6.

[37] V.V. Zhakhovskii, N.A. Inogamov, Y.V. Petrov, S.I. Ashitkov, K. Nishihara, Molecular dynamics simulation of femtosecond ablation and spallation with different interatomic potentials, Appl. Surf. Sci. 255 (24) (2009) 9592–9596, https://doi.org/10.1016/j.apsusc.2009.04.082.

[38] C.R. Dandekar, Y.C. Shin, Molecular dynamics based cohesive zone law for describing Al–SiC interface mechanics, Compos. Part A Appl. Sci. Manuf. 42 (4) (2011) 355–363, https://doi.org/10.1016/j.compositesa.2010.12.005.

[39] A.P. Thompson, H.M. Aktulga, R. Berger, D.S. Bolintineanu, W.M. Brown, P. S. Crozier, P.J. in 't Veld, A. Kohlmeyer, S.G. Moore, T.D. Nguyen, R. Shan, M. J. Stevens, J. Tranchida, C. Trott, S.J. Plimpton, LAMMPS - a flexible simulation tool for particle-based materials modeling at the atomic, meso, and continuum scales, Comput. Phys. Commun. 271 (2022), https://doi.org/10.1016/j.cpc.2021.108171.

[40] A. Stukowski, Visualization and analysis of atomistic simulation data with OVITO–the Open Visualization Tool, Model. Simul. Mat. Sci. Eng. 18 (1) (2010) 015012, https://doi.org/10.1088/0965-0393/18/1/015012.

[41] R. Devanathan, W.J. Weber, Displacement energy surface in 3C and 6H SiC, J. Nucl. Mater. 278 (2–3) (2000) 258–265, https://doi.org/10.1016/s0022-3115(99)00266-4.

[42] M.J. Madito, T.T. Hlatshwayo, C.B. Mtshali, Chemical disorder of a-SiC layer induced in 6H-SiC by Cs and I ions co-implantation: Raman spectroscopy analysis, Appl. Surf. Sci. 538 (2021), https://doi.org/10.1016/j.apsusc.2020.148099.

[43] E.S. Gadelmawla, M.M. Koura, T.M.A. Maksoud, I.M. Elewa, H.H. Soliman, Roughness parameters, J. Mater. Process. Technol. 123 (1) (2002) 133–145, https://doi.org/10.1016/s0924-0136(02)00060-2.

[44] S. Magalhães, J.G. Ramos, D.N. Faye, D.M. Esteves, D.R. Pereira, M. Peres, G. Gupta, S. Rath, K. Lorenz, Compositional mapping of ion implantation damage in $Al_{1-x}Ga_xN$ via a two-step high-resolution X-ray diffraction simulation, Phys. Status Solidi (RRL) – Rapid Res. Lett. (2025), https://doi.org/10.1002/pssr.202500144.

[45] A. Sharmila, N. Pandey, S. Singh, G. Dalal, P.S.K. Gupta, Structural and spectroscopic properties of nitrogen ion-implanted GaN epitaxial layers, J. Mater. Chem. C 36 (16) (2025), https://doi.org/10.1007/s10854-025-14945-2.

[46] S.Z. Chavoshi, X. Luo, Molecular dynamics simulation study of deformation mechanisms in 3C–SiC during nanometric cutting at elevated temperatures, Mater. Sci. Eng. A 654 (2016) 400–417, https://doi.org/10.1016/j.msea.2015.11.100.

[47] X. Luo, S. Goel, R.L. Reuben, A quantitative assessment of nanometric machinability of major polytypes of single crystal silicon carbide, J. Eur. Ceram. Soc. 32 (12) (2012) 3423–3434, https://doi.org/10.1016/j.jeurceramsoc.2012.04.016.

[48] M.K. Linnarsson, A. Hallén, L. Vines, Intentional and unintentional channeling during implantation of ^{51}V ions into 4H-SiC, Semicond. Sci. Technol. 34 (11) (2019), https://doi.org/10.1088/1361-6641/ab4163.

[49] J. Müting, V. Bobal, L. Vines, U. Grossner, Phosphorus implantation into 4H-SiC at room and elevated temperature, Semicond. Sci. Technol. 36 (6) (2021), https://doi.org/10.1088/1361-6641/abf55a.

[50] S. Pal, M. Meraj, C. Deng, Effect of Zr addition on creep properties of ultra-fine grained nanocrystalline Ni studied by molecular dynamics simulations, Comput. Mater. Sci 126 (2017) 382–392, https://doi.org/10.1016/j.commatsci.2016.10.013.

[51] R. Devanathan, T.D.d. Rubia, W.J. Weber, Displacement threshold energies in β-SiC, J. Nucl. Mater. 253 (1998) 47–52, https://doi.org/10.1016/S0022-3115(97)00304-8.

[52] N. Sellami, A. Debelle, M.W. Ullah, H.M. Christen, J.K. Keum, H. Bei, H. Xue, W. J. Weber, Y. Zhang, Effect of electronic energy dissipation on strain relaxation in irradiated concentrated solid solution alloys, Curr. Opin. Solid State Mater. Sci. 23 (2) (2019) 107–115, https://doi.org/10.1016/j.cossms.2019.02.002.

[53] M.K. Linnarsson, L. Vines, A. Hallén, Influence from the electronic shell structure on the range distribution during channeling of 40–300 keV ions in 4H-SiC, J. Appl. Phys. 130 (7) (2021), https://doi.org/10.1063/5.0054188.

[54] G.W. Egeland, J.A. Valdez, S.A. Maloy, K.J. McClellan, K.E. Sickafus, G.M. Bond, Heavy-ion irradiation defect accumulation in ZrN characterized by TEM, GIXRD, nanoindentation, and helium desorption, J. Nucl. Mater. 435 (1–3) (2013) 77–87, https://doi.org/10.1016/j.jnucmat.2012.12.025.

[55] A.A. Ali, J. Kumar, V. Ramakrishnan, K. Asokan, Raman spectroscopic study of He ion implanted 4H and 6H-SiC, Mater. Lett. 213 (2018) 208–210, https://doi.org/10.1016/j.matlet.2017.11.040.

[56] X. Ban, Z. Tian, S. Zheng, J. Zhu, W. Ba, N. Wang, S. Han, H. Qiu, X. Wang, Z. Li, Scratching properties of 4H-SiC single crystal after oxidation under different conditions, Wear (2024), https://doi.org/10.1016/j.wear.2024.205503.

[57] R. Sugie, T. Uchida, Determination of stress components in 4H-SiC power devices via Raman spectroscopy, J. Appl. Phys. 122 (19) (2017), https://doi.org/10.1063/1.5003613.

[58] X. Luo, X. Lu, C. Cong, T. Yu, Q. Xiong, S.Y. Quek, Stacking sequence determines Raman intensities of observed interlayer shear modes in 2D layered materials - a general bond polarizability model, Sci. Rep. 5 (2015) 14565, https://doi.org/10.1038/srep14565.

[59] P. Zhang, J. Fan, Y. Wang, Y. Dang, S. Heumann, Y. Ding, Insights into the role of defects on the Raman spectroscopy of carbon nanotube and biomass-derived carbon, Carbon 222 (2024) 118998, https://doi.org/10.1016/j.carbon.2024.118998.

[60] L. Zhang, W. Jiang, C. Pan, R.C. Fadanelli, W. Ai, L. Chen, T. Wang, Raman study of amorphization in nanocrystalline 3C–SiC irradiated with C^+ and He^+ ions, J. Raman Spectrosc. 50 (8) (2019) 1197–1204, https://doi.org/10.1002/jrs.5631.

[61] K. Piskorski, M. Guziewicz, M. Wzorek, L. Dobrzański, Investigation of Al- and N-implanted 4H–SiC applying visible and deep UV Raman scattering spectroscopy, AIP Adv. 10 (5) (2020), https://doi.org/10.1063/1.5144579.

[62] H. Yuan, P. Zhang, F. Gao, Compressive hyperspectral Raman imaging via randomly interleaved scattering projection, Optica 8 (11) (2021), https://doi.org/10.1364/optica.438826.

[63] Z. Yang, X. Wang, W. Chen, H. Tang, R. Zhang, X. Fan, G. Zhang, J. Fan, Residual stress characterization in microelectronic manufacturing: an analysis based on Raman spectroscopy, Laser & Photon. Rev. 18 (7) (2024) 2301300, https://doi.org/10.1002/lpor.202301300.

[64] N.T. Dang, D.P. Kozlenko, O.N. Lis, S.E. Kichanov, Y.V. Lukin, N.O. Golosova, B. N. Savenko, D.L. Duong, T.L. Phan, T.A. Tran, M.H. Phan, High pressure-driven magnetic disorder and structural transformation in Fe_3GeTe_2 : emergence of a magnetic quantum critical poin, Adv. Sci. 10 (9) (2023) e2206842, https://doi.org/10.1002/advs.202206842.

[65] S.K. Saxena, R. Borah, V. Kumar, H.M. Rai, R. Late, V.G. Sathe, A. Kumar, P. R. Sagdeo, R. Kumar, Raman spectroscopy for study of interplay between phonon confinement and Fano effect in silicon nanowires, J. Raman Spectrosc. 47 (3) (2016) 283–288, https://doi.org/10.1002/jrs.4820.

[66] M. Tanwar, R. Kumar, Effect of dimensionality on the excitation wavelength dependence of the Fano-Raman line-shape: a brief review, Nanoscale 16 (13) (2024) 6429–6441, https://doi.org/10.1039/d3nr00445g.

[67] A.J. Leide, R.I. Todd, D.E.J. Armstrong, Measurement of swelling-induced residual stress in ion implanted SiC, and its effect on micromechanical properties, Acta Mater. 196 (2020) 78–87, https://doi.org/10.1016/j.actamat.2020.06.030.

[68] J. Li, Transformation strain by chemical disordering in silicon carbide, J. Appl. Phys. 95 (11) (2004) 6466–6469, https://doi.org/10.1063/1.1690093.

[69] X. Qin, X. Li, X. Chen, X. Yang, F. Zhang, X. Xu, X. Hu, Y. Peng, P. Yu, Raman scattering study on phonon anisotropic properties of SiC, J. Alloys Compd. 776 (2019) 1048–1055, https://doi.org/10.1016/j.jallcom.2018.10.324.
[70] B. Han, M. Sun, Y. Chang, S. He, Y. Zhao, C. Qu, W. Qiu, Raman characterization of the in-Plane stress tensor of gallium nitride, Materials (basel) 16 (6) (2023) 2255, https://doi.org/10.3390/ma16062255.
[71] Z. Yang, X. Wang, Y. Zuo, Z. Tang, B. Guo, J. Zhang, H. Tang, R. Zhang, X. Fan, G. Zhang, J. Fan, Prediction of temperature-dependent stress in 4H-SiC using in situ nondestructive Raman spectroscopy characterization, Laser & Photon. Rev. 19 (3) (2024), https://doi.org/10.1002/lpor.202401033.